JACS
JOURNAL OF THE AMERICAN CHEMICAL SOCIETY
Cite This: J. Am. Chem. Soc. 2019, 141, 18395−18399
Communication
pubs.acs.org/JACS

Redox-Sensitive Facet Dependency in Etching of Ceria Nanocrystals Directly Observed by Liquid Cell TEM

Jongbaek Sung,[†,‡,⊥] Back Kyu Choi,[†,‡,⊥] Byunghoon Kim,[†,§] Byung Hyo Kim,[†,‡] Joodeok Kim,[†,‡] Donghoon Lee,[†,‡] Sungin Kim,[†,‡] Kisuk Kang,*[,†,§,∥] Taeghwan Hyeon,*[,†,‡] and Jungwon Park*[,†,‡]

[†]Center for Nanoparticle Research, Institute for Basic Science (IBS), Seoul 08826, Republic of Korea

[‡]School of Chemical and Biological Engineering, and Institute of Chemical Process, Seoul National University, Seoul 08826, Republic of Korea

[§]Department of Materials Science and Engineering, and Research Institute of Advanced Materials, Seoul National University, Seoul 08826, Republic of Korea

[∥]Institute of Engineering Research, College of Engineering, Seoul National University, Seoul 08826, Republic of Korea

Supporting Information

ABSTRACT: Defining the redox activity of different surface facets of ceria nanocrystals is important for designing an efficient catalyst. Especially in liquid-phase reactions, where surface interactions are complicated, direct investigation in a native environment is required to understand the facet-dependent redox properties. Using liquid cell TEM, we herein observed the etching of ceria-based nanocrystals under the control of redox-governing factors. Direct nanoscale observation reveals facet-dependent etching kinetics, thus identifying the specific facet ({100} for reduction and {111} for oxidation) that governs the overall etching under different chemical conditions. Under each redox condition, the contribution of the predominant facet increases as the etching reactivity increases.

Ceria (CeO_2) is a widely used catalytic material in both gas- and liquid-phase reactions owing to its unique redox property.[1] The low redox potential of Ce^{4+}/Ce^{3+} enables facile switching between them, compensated by the lattice oxygen transport to the surrounding environment. Such lability of the redox states of ceria varies according to different facets because the coordination numbers of surface atoms are facet-dependent. Indeed, controlling the ratio of the active surfaces is the key criterion in synthesizing ceria-based catalytic nanomaterials.[2] Among the three most abundant surfaces of ceria, the {111} surface has the most highly coordinated structure which results in the lowest activity to form oxygen vacancy, followed by {100} and {110}.[3] Thus, surface reducibility increases in the order of {111}, {100}, and {110}, as observed by the different Ce^{3+}/Ce^{4+} ratios on those facets.[4] Diverse approaches have been utilized to understand the redox activities of those facets, however, mostly limited to gas phase systems.[3,5]

The valence states and surface structures of ceria fluctuate dynamically by their interaction with chemical species during redox reactions.[6] For example, gaseous CO_2 and O_2 suppresses the mobility of surface Ce atoms by altering surface termination.[7] The surface redox properties and facet-dependent activity of ceria is presumably more complicated in liquid-phase reactions because of the frequent interactions with molecules in solution. The redox activity of ceria is readily modified by interactions with H_2O.[8] Complex diffusion dynamics also result in various Ce^{3+}/Ce^{4+} compositions during catalytic cycles.[9] Consequently, to understand the complex surface activity of ceria in liquid-phase catalytic reactions, a method to directly observe the redox behaviors of different surfaces in a chemically controlled liquid is required.

The development of liquid cell TEM (LCTEM) has enabled the real-time observation of chemical reactions of nanoparticles.[10] In particular, recent LCTEM studies have shown that reducible oxides undergo dissolution by surface reduction.[11] Herein, we use LCTEM to investigate facet-dependent etching of ceria-based nanocrystals with controlling major redox-governing factors such as cationic alloying and the oxidizing power of the liquid. Quantitative analyses of individual nanocrystal etching combined with first-principles calculations elucidate that the predominant contribution of active facet governs the overall etching rate, regardless of the different mechanistic pathways.

Crystalline ceria and ceria-zirconia (CeO_2−ZrO_2) nanocrystals dispersed in H_2O, denoted as Ce/H_2O and CZ/H_2O respectively, were loaded in a static-type liquid cell to image their etching, as shown in Figure 1a and Movies S1−S2 (Figures S1 and S2, Supporting Information). Introducing a small Zr^{4+} ion into ceria is known to enhance the oxygen storage capacity by facilitating lattice oxygen transport.[1b,12] In addition, the etching of ceria nanocrystals in an oxidative environment was also studied with ceria dispersed in 30% $H_2O_{2(aq)}$, denoted as Ce/H_2O_2 (Movie S3). Among nanocrystals observed in the field of view, isolated particles of ∼25 nm in size, and showing parallelogram projection with a similar degree of truncation at the corners, were selected to quantitatively compare the etching of the same surface under different chemical conditions (Figure S3, Table S1). Aberration-corrected TEM images verify that the morphology of the selected nanocrystal is a typical ceria nano-octahedra,

Received: September 3, 2019
Published: October 23, 2019

DOI: 10.1021/jacs.9b09508
J. Am. Chem. Soc. 2019, 141, 18395−18399

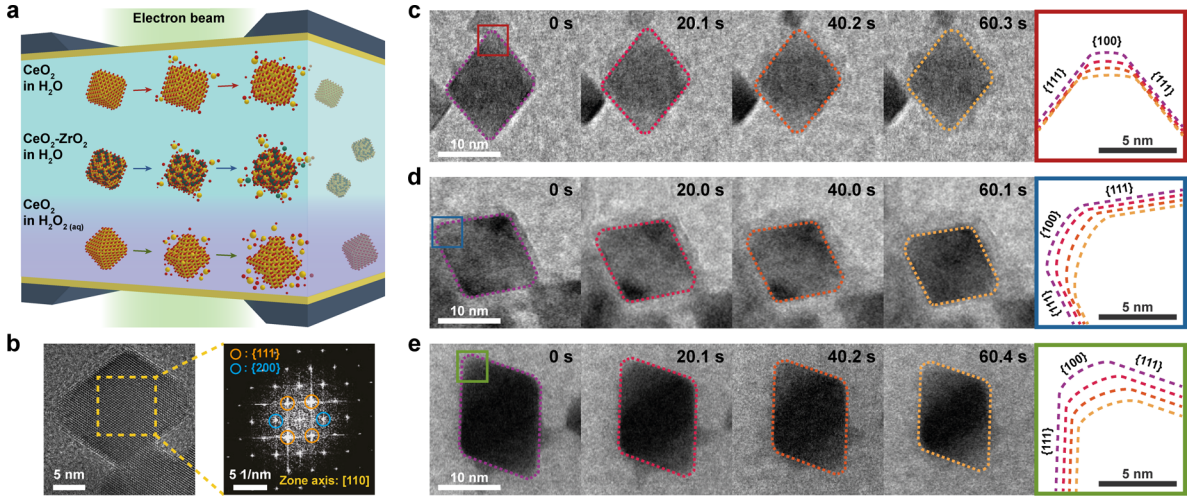

Figure 1. (a) Illustration of ceria-based nanocrystals etching in LCTEM. (b) Aberration-corrected TEM image and corresponding fast Fourier transform pattern of ceria nanocrystal. (c–e) Time-series etching trajectories and the local magnified contours of selected nanocrystals. (c) Ce/H_2O, (d) CZ/H_2O, and (e) Ce/H_2O_2.

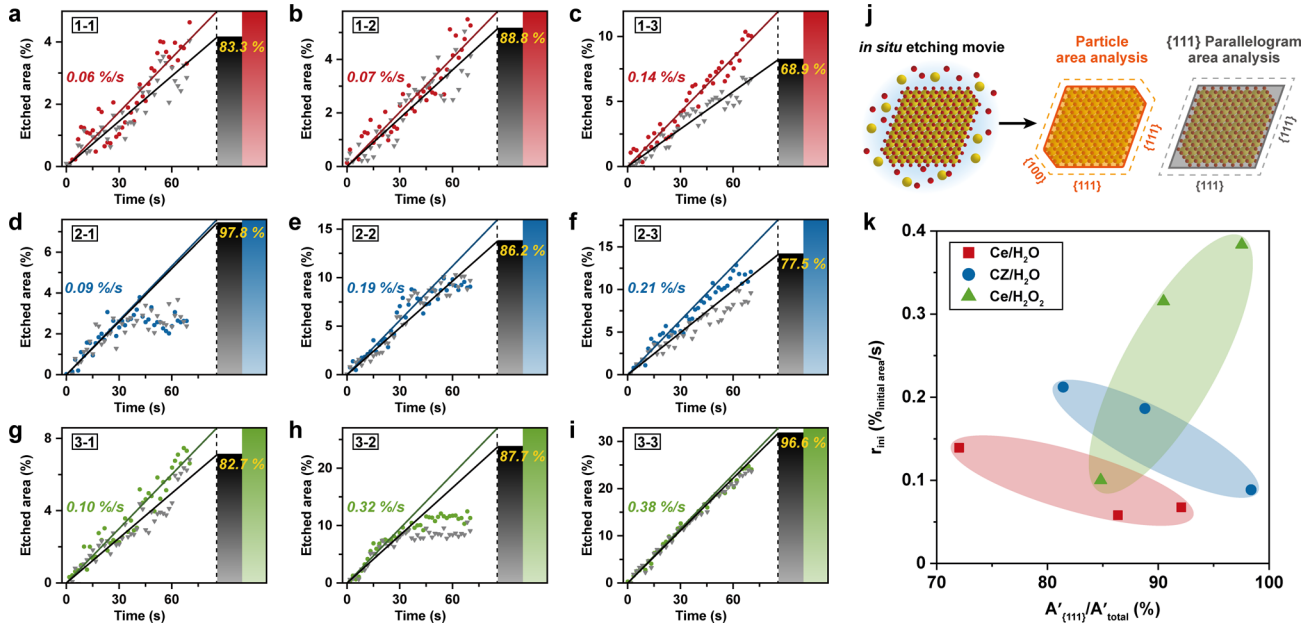

Figure 2. (a–i) The amount of etched area per initial particle area in time, for particles in (a–c) Ce/H_2O, (d–f) CZ/H_2O, and (g–i) Ce/H_2O_2. The r_{ini} and etched area of the original projected particle are color-coded. The etched area of {111} parallelogram is depicted as gray symbols. The bar chart illustrates the etching rate ratio of original projected area to {111} parallelogram. (j) Illustration of the etching rate analysis. (k) r_{ini} as a function of {111} surface contribution, $A'_{\{111\}}/A'_{total}$.

consisting {111} faces with {100} truncation at corner sites (Figure 1b, Figures S4–S7).[4a,13]

The representative etching of nanocrystals with the fastest etching rate among several trajectories measured in Ce/H_2O, CZ/H_2O and Ce/H_2O_2 are shown in Figure 1c, 1d, and 1e, respectively (Movies S1–S3). The main edges of {111} and truncated facets of {100} mainly contribute to the overall etching, while the etching of the {110} facet, corners with obtuse angles, is insignificant in all cases. The magnified etching trajectories shown in Figure 1c–e indicate that the overall surface-dependent etching behaviors vary significantly according to the different conditions regulated by lattice oxygen lability and redox environment. For both Ce/H_2O and CZ/H_2O, the etching of the truncated facet at the corner ({100}) is more pronounced than the case of Ce/H_2O_2 that undergoes relatively homogeneous etching along the perimeter. Consequently, our LCTEM observations confirm that the etching of ceria-based nanocrystals in solution is sensitive to both the local surface structure and reaction conditions.

We quantified the etching rate of ceria-based nanocrystals by extracting the projected area in time-series TEM images (colored symbols in Figure 2a–i). Using a statistical method, the initial etching rate (r_{ini}) of each nanocrystal was calculated, as shown in Figure 2a–i (Table S2, Supporting Information). For every nanocrystal, the amount of etched area increases linearly over 40 s, consistent with the previously reported observations.[14] In the later stage, a film is observed around the particle surface, which is presumably a diffuse layer formed from the etched species.[11c,15] To further understand the etching dynamics and the corresponding redox properties of

DOI: 10.1021/jacs.9b09508
J. Am. Chem. Soc. 2019, 141, 18395–18399

different facets, we compared the areal change of the '{111} parallelogram' (a parallelogram constructed by extending the {111} surface of the nanocrystal) to that of the original projected area (Figure 2j). Since shrinking of this parallelogram excludes the etching at the truncated {100} corner, the etching rate of the parallelogram solely represents {111} surface etching and is, therefore, always smaller than the etching rate of the original projected area. Along with the etched area of the original particle, the etched area of the {111} parallelogram is also depicted in Figure 2a–i.

We note that the etching rates of individual nanocrystals under the same chemical conditions are heterogeneous (Figure 2a–i).[16] More interestingly, the trend of r_{ini} under each case correlates with the relative contributions of different facets. The etching rate ratios of the {111} parallelogram to the original projected area (bar charts in Figure 2a–i) represent the degree of etching along {111} facets. For Ce/H_2O, the etching rate ratios are ~86% when the r_{ini} is small, but the ratio significantly decreases to 68.9% as the r_{ini} is doubled to 0.14%/s (Figure 2a–c). A similar trend in the etching rate ratio and the r_{ini} is observed in CZ/H_2O (Figure 2d–f). In contrast, for Ce/H_2O_2, the etching rate ratio increases from 82.7% to 96.6% as the r_{ini} increases (Figure 2g–i). We deconvoluted the actual etching contribution of the {111} facet by mathematical conversion of the etching rate ratio of the {111} parallelogram and original projected area (Supporting Information). Figure 2k shows a plot of the ratio of the actual percentages of {111} surface etching and the overall etching, denoted as $A'_{\{111\}}/A'_{total}$, and the r_{ini}. For both Ce/H_2O and CZ/H_2O, the initial etching is faster as {111} facets contribute less, and {100} facets contribute more to the overall etching. An opposite trend is observed for Ce/H_2O_2. Therefore, the overall etching kinetics is mainly governed by the predominant contribution of specific facets in different chemical conditions ({100} for Ce/H_2O and CZ/H_2O, {111} for Ce/H_2O_2). We also confirm that the observed facet predominance is still evident under different electron beam dose rate (Figures S8 and S9).

Our LCTEM observations allowed us to understand nanocrystal etching at a level that resolves individual facet contributions, and to identify the predominant facet governing the etching rate under each condition. Regardless of this complexity, there are significant differences in the overall activity under three reaction conditions. Among nanocrystals with almost identical sizes, the etching rates in CZ/H_2O and Ce/H_2O_2 are faster than that in Ce/H_2O (Figure 3a). Enhancement of the r_{ini} for CZ/H_2O and Ce/H_2O_2 is also evident when three r_{ini} for each case in Figure 2a–i are averaged (Figure 3b). Also by comparing the r_{ini} of the particles with similar $A'_{\{111\}}/A'_{total}$ values of ~90% (Figure 2k), we conclude that the cationic alloying of Zr and the oxidizing power of H_2O_2 enhance the etching reactivity of ceria nanocrystals.

The effect of Zr alloying on etching was investigated through *ex situ* energy dispersive X-ray spectroscopy (EDS) of etched CeO_2–ZrO_2 nanocrystals. The atomic ratio of Ce to Zr at the nanocrystal core and the diffuse layer are 50:50 and 70:30, respectively, indicating that Zr is less prone to etching than Ce (Figures 3c and S10). Elemental maps of Ce and Zr also indicate that Zr localizes within the nanocrystal, while Ce is widely distributed over the nanocrystal boundary (Figure 3c). This result implies that the enhanced etching rate of CZ/H_2O is not due to Zr dissolution. Instead, Zr alloying enhances the

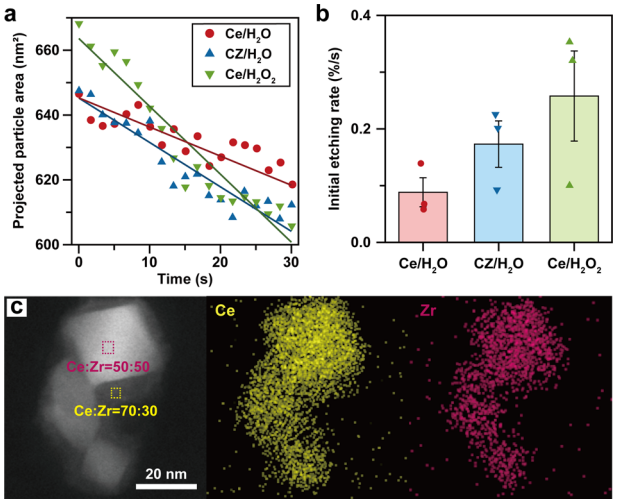

Figure 3. (a) Projected areal change of nanocrystals with similar sizes and (b) averaged r_{ini} of nanocrystals, in three cases. (c) EDS elemental mapping of etched CeO_2–ZrO_2 nanocrystals. Composition mapping was performed in selected regions.

lattice oxygen lability,[1b,12] which presumably increases the etching rate.

In general, etching of ceria-based nanomaterials occurs universally in redox-active conditions, as confirmed by the reductive etching of CeO_2 from *ex situ* experiments (Figure S11). The release of lattice oxygen by surface reduction under LCTEM imaging is the process governing the etching of Ce/H_2O and CZ/H_2O (Figure S12).[17] First-principles calculations clearly indicate the lowering of the Ce binding energy at (100) and (111) surfaces by surface reduction of Ce^{4+} to Ce^{3+} (Figure 4), consistent with the previous study.[11a] Therefore,

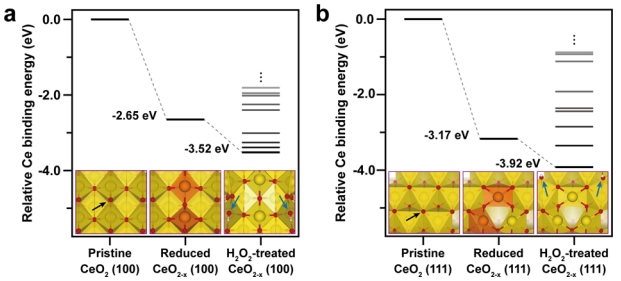

Figure 4. First-principles calculation of Ce binding energies at representative (a) (100) and (b) (111) surfaces. The Ce binding energy on pristine surfaces is set to 0 eV. The red, yellow, and orange balls represent O^{2-}, Ce^{4+}, and Ce^{3+}, respectively. The black arrow in the pristine CeO_2 indicates the vacancy site at CeO_{2-x}. The blue arrows in H_2O_2-treated CeO_{2-x} indicate the representative location of OH^- ions with lower Ce binding energy compared to that of reduced CeO_{2-x}.

the reductive etching of ceria-based nanocrystals in H_2O can be understood as a process of losing surface lattice oxygen and cerium due to the lowered binding energy of surface Ce^{3+}. For such surface reduction, {100} surfaces are more active than {111} surfaces.[3] The {100} surfaces are the ones that react more predominantly as the r_{ini} increases, as shown in Figure 2k. The increment of {100} predominance is probably due to the crystallographic nature of different surfaces. Owing to the sparsely located surface oxygens on {100}, repulsion between oxygen vacancies generated from reduction is less significant

DOI: 10.1021/jacs.9b09508
J. Am. Chem. Soc. 2019, 141, 18395–18399

than on {111}. Thus, oxygen vacancies at {100} can be more easily accommodated as the etching rate increases.[3a]

In the Ce/H_2O_2 case, surface Ce^{3+} creation during LCTEM imaging and oxidation of Ce^{3+} by H_2O_2 occur simultaneously, producing surface Ce^{4+} and OH^- ions (Figure S13).[9] To describe this situation, we calculated the Ce binding energies for H_2O_2-treated CeO_{2-x} surfaces with various configurations of OH^- ions (right sections in Figure 4a–b). The Ce binding energies are predicted to depend on the location of OH^- ions (Table S3). Interestingly, the presence of OH^- ions near the surface allows surface Ce^{4+} ions to have much lower binding energies compared to that of reduced CeO_{2-x} (middle sections of Figure 4a–b). In addition, the release of Ce^{4+} at H_2O_2-treated surfaces results in the formation of superoxo/peroxo species, indicated by the short O–O distance in Table S4 (Figures S14–S15), which may also expedite the etching. Therefore, the addition of the oxidation step to the overall etching pathway converts the reduced surface Ce^{3+} to weakly coordinated Ce^{4+}, accelerating the overall etching of Ce/H_2O_2.

The calculated work functions for the reduced (111) surface (4.95 eV) and reduced (100) surface (6.04 eV) indicate that the reduced {111} surface is more active toward oxidation. {111} is also the most active surface that predominantly participates in etching as the overall activity increases in Ce/H_2O_2 (Figure 2k). We believe that the surface structure of {111} plays a key role in stabilizing the excess charge of oxidized Ce^{4+}. Since the coordination number (CN) of Ce on the {111} surface (CN = 7) is higher than that of the {100} surface (CN = 6), {111} can more effectively dissipate the excess charge than {100}.[1a] The ease of forming additional surface Ce^{4+} can increase the predominance of {111} in an oxidative environment.

In summary, we report the different etching behaviors of ceria-based nanocrystals under the control of redox-governing factors using LCTEM. The analysis of the etching behavior at the facet level reveals that the predominance of an active facet governs the overall etching rate, under both reductive and oxidative conditions. The experimental platform introduced here can be extensively exploited to understand the redox properties of nanomaterials in realistic liquid environments.

■ ASSOCIATED CONTENT

Supporting Information

The Supporting Information is available free of charge on the ACS Publications website at DOI: 10.1021/jacs.9b09508.

Materials and methods, computational details, and supporting figures and tables (PDF)

Movie S1: *in situ* LCTEM movie of CeO_2 nanocrystals etching under H_2O environment (MP4)

Movie S2: *in situ* LCTEM movie of CeO_2–ZrO_2 nanocrystals etching under H_2O environment (MP4)

Movie S3: *in situ* LCTEM movie of CeO_2 nanocrystals etching under $H_2O_{2(aq)}$ environment (MP4)

■ AUTHOR INFORMATION

Corresponding Authors

* matlgen1@snu.ac.kr (K.K.)
* thyeon@snu.ac.kr (T.H.)
* jungwonpark@snu.ac.kr (J.P.)

ORCID

Jongbaek Sung: 0000-0002-9294-3246
Byung Hyo Kim: 0000-0002-4098-0053
Kisuk Kang: 0000-0002-8696-1886
Taeghwan Hyeon: 0000-0001-5959-6257
Jungwon Park: 0000-0003-2927-4331

Author Contributions

⊥J.S. and B.K.C. contributed equally.

Notes

The authors declare no competing financial interest.

■ ACKNOWLEDGMENTS

This work was supported by IBS-R006-D1. J.P. acknowledges the National Research Foundation of Korea (NRF) grant funded by the Korea government (MSIT) (No. NRF-2017R1C1B2010434, No. NRF-2017R1A5A1015365, and NRF-2019M3E6A1064877). J.S. and J.P. acknowledge support by the Samsung Science and Technology Foundation under Project number SSTF-BA1802-08 for the method development for data analysis and characterization. K.K. acknowledges the support of IBS-R006-A2 and the NRF grant funded by the Korea government (MSIP) (2018R1A2A1A05079249). We thank Insung Kong for providing statistical backgrounds.

■ REFERENCES

(1) (a) Trovarelli, A.; Llorca, J. Ceria Catalysts at Nanoscale: How Do Crystal Shapes Shape Catalysis? *ACS Catal.* **2017**, *7* (7), 4716–4735. (b) Montini, T.; Melchionna, M.; Monai, M.; Fornasiero, P. Fundamentals and Catalytic Applications of CeO2-Based Materials. *Chem. Rev.* **2016**, *116* (10), 5987–6041.

(2) (a) Vile, G.; Colussi, S.; Krumeich, F.; Trovarelli, A.; Perez-Ramirez, J. Opposite Face Sensitivity of CeO2 in Hydrogenation and Oxidation Catalysis. *Angew. Chem., Int. Ed.* **2014**, *53* (45), 12069–12072. (b) Wang, D. Y.; Kang, Y. J.; Doan-Nguyen, V.; Chen, J.; Kungas, R.; Wieder, N. L.; Bakhmutsky, K.; Gorte, R. J.; Murray, C. B. Synthesis and Oxygen Storage Capacity of Two-Dimensional Ceria Nanocrystals. *Angew. Chem., Int. Ed.* **2011**, *50* (19), 4378–4381. (c) Yu, T.; Lim, B.; Xia, Y. N. Aqueous-Phase Synthesis of Single-Crystal Ceria Nanosheets. *Angew. Chem., Int. Ed.* **2010**, *49* (26), 4484–4487. (d) Wang, D. Y.; Kang, Y. J.; Ye, X. C.; Murray, C. B. Mineralizer-Assisted Shape-Control of Rare Earth Oxide Nanoplates. *Chem. Mater.* **2014**, *26* (22), 6328–6332. (e) Wu, Z. L.; Li, M. J.; Overbury, S. H. On the structure dependence of CO oxidation over CeO2 nanocrystals with well-defined surface planes. *J. Catal.* **2012**, *285* (1), 61–73. (f) Wang, Y. H.; Wang, F.; Song, Q.; Xin, Q.; Xu, S. T.; Xu, J. Heterogeneous Ceria Catalyst with Water-Tolerant Lewis Acidic Sites for One-Pot Synthesis of 1,3-Diols via Prins Condensation and Hydrolysis Reactions. *J. Am. Chem. Soc.* **2013**, *135* (4), 1506–1515.

(3) (a) Paier, J.; Penschke, C.; Sauer, J. Oxygen Defects and Surface Chemistry of Ceria: Quantum Chemical Studies Compared to Experiment. *Chem. Rev.* **2013**, *113* (6), 3949–3985. (b) Fabris, S.; Vicario, G.; Balducci, G.; de Gironcoli, S.; Baroni, S. Electronic and atomistic structures of clean and reduced ceria surfaces. *J. Phys. Chem. B* **2005**, *109* (48), 22860–22867. (c) Nolan, M.; Parker, S. C.; Watson, G. W. The electronic structure of oxygen vacancy defects at the low index surfaces of ceria. *Surf. Sci.* **2005**, *595* (1–3), 223–232.

(4) (a) Goris, B.; Turner, S.; Bals, S.; Van Tendeloo, G. Three-Dimensional Valency Mapping in Ceria Nanocrystals. *ACS Nano* **2014**, *8* (10), 10878–10884. (b) Turner, S.; Lazar, S.; Freitag, B.; Egoavil, R.; Verbeeck, J.; Put, S.; Strauven, Y.; Van Tendeloo, G. High resolution mapping of surface reduction in ceria nanoparticles. *Nanoscale* **2011**, *3* (8), 3385–3390.

(5) (a) Wu, Z. L.; Mann, A. K. P.; Li, M. J.; Overbury, S. H. Spectroscopic Investigation of Surface-Dependent Acid Base Property of Ceria Nanoshapes. *J. Phys. Chem. C* **2015**, *119* (13), 7340–7350. (b) Zhang, L.; Ma, K.; Shao, C.; Tang, Z.; Cheng, Q. P.; An, P. F.; Chu, S. Q.; Zheng, L. R.; Li, X. G.; Zhang, J. Unraveling the Low-Temperature Redox Behavior of Ultrathin Ceria Nanosheets with

DOI: 10.1021/jacs.9b09508
J. Am. Chem. Soc. 2019, 141, 18395–18399

Exposed {110} Facets by in Situ XAFS/DRIFTS Utilizing CO as Molecule Probe. *J. Phys. Chem. C* **2019**, *123* (1), 322−333. (c) Schilling, C.; Ganduglia-Pirovano, M. V.; Hess, C. Experimental and Theoretical Study on the Nature of Adsorbed Oxygen Species on Shaped Ceria Nanoparticles. *J. Phys. Chem. Lett.* **2018**, *9* (22), 6593−6598.

(6) Crozier, P. A.; Wang, R. G.; Sharma, R. In situ environmental TEM studies of dynamic changes in cerium-based oxides nanoparticles during redox processes. *Ultramicroscopy* **2008**, *108* (11), 1432−1440.

(7) Bugnet, M.; Overbury, S. H.; Wu, Z. L.; Epicier, T. Direct Visualization and Control of Atomic Mobility at {100} Surfaces of Ceria in the Environmental Transmission Electron Microscope. *Nano Lett.* **2017**, *17* (12), 7652−7658.

(8) Sayle, T. X. T.; Molinari, M.; Das, S.; Bhatta, U. M.; Mobus, G.; Parker, S. C.; Seal, S.; Sayle, D. C. Environment-mediated structure, surface redox activity and reactivity of ceria nanoparticles. *Nanoscale* **2013**, *5* (13), 6063−6073.

(9) (a) Malyukin, Y.; Maksimchuk, P.; Seminko, V.; Okrushko, E.; Spivak, N. Limitations of Self-Regenerative Antioxidant Ability of Nanoceria Imposed by Oxygen Diffusion. *J. Phys. Chem. C* **2018**, *122* (28), 16406−16411. (b) Karakoti, A. S.; Singh, S.; Kumar, A.; Malinska, M.; Kuchibhatla, S. V. N. T.; Wozniak, K.; Self, W. T.; Seal, S. PEGylated Nanoceria as Radical Scavenger with Tunable Redox Chemistry. *J. Am. Chem. Soc.* **2009**, *131* (40), 14144−14145.

(10) (a) Kim, J.; Jones, M. R.; Ou, Z. H.; Chen, Q. In Situ Electron Microscopy Imaging and Quantitative Structural Modulation of Nanoparticle Superlattices. *ACS Nano* **2016**, *10* (11), 9801−9808. (b) Wu, J. B.; Gao, W. P.; Yang, H.; Zuo, J. M. Dissolution Kinetics of Oxidative Etching of Cubic and Icosahedral Platinum Nanoparticles Revealed by in Situ Liquid Transmission Electron Microscopy. *ACS Nano* **2017**, *11* (2), 1696−1703. (c) Kim, B. H.; Yang, J.; Lee, D.; Choi, B. K.; Hyeon, T.; Park, J. Liquid-Phase Transmission Electron Microscopy for Studying Colloidal Inorganic Nanoparticles. *Adv. Mater.* **2018**, *30* (4), 1703316. (d) Liang, W. I.; Zhang, X. W.; Zan, Y. L.; Pan, M.; Czarnik, C.; Bustillo, K.; Xu, J.; Chu, Y. H.; Zheng, H. M. In Situ Study of Fe3Pt-Fe2O3 Core-Shell Nanoparticle Formation. *J. Am. Chem. Soc.* **2015**, *137* (47), 14850−14853. (e) Chen, Q.; Smith, J. M.; Park, J.; Kim, K.; Ho, D.; Rasool, H. I.; Zettl, A.; Alivisatos, A. P. 3D Motion of DNA-Au Nanoconjugates in Graphene Liquid Cell Electron Microscopy. *Nano Lett.* **2013**, *13* (9), 4556−4561. (f) Gao, W. P.; Hou, Y. S.; Hood, Z. D.; Wang, X.; More, K.; Wu, R. Q.; Xia, Y. N.; Pan, X. Q.; Chi, M. F. Direct in Situ Observation and Analysis of the Formation of Palladium Nanocrystals with High-Index Facets. *Nano Lett.* **2018**, *18* (11), 7004−7013. (g) Niu, K. Y.; Park, J.; Zheng, H. M.; Alivisatos, A. P. Revealing Bismuth Oxide Hollow Nanoparticle Formation by the Kirkendall Effect. *Nano Lett.* **2013**, *13* (11), 5715−5719. (h) Wu, J. B.; Gao, W. P.; Wen, J. G.; Miller, D. J.; Lu, P.; Zuo, J. M.; Yang, H. Growth of Au on Pt Icosahedral Nanoparticles Revealed by Low-Dose In Situ TEM. *Nano Lett.* **2015**, *15* (4), 2711−2715.

(11) (a) Lu, Y.; Geng, J. G.; Wang, K.; Zhang, W.; Ding, W. Q.; Zhang, Z. H.; Xie, S. H.; Dai, H. X.; Chen, F. R.; Sui, M. L. Modifying Surface Chemistry of Metal Oxides for Boosting Dissolution Kinetics in Water by Liquid Cell Electron Microscopy. *ACS Nano* **2017**, *11* (8), 8018−8025. (b) Asghar, M. S. A.; Inkson, B. J.; Mobus, G. Giant Radiolytic Dissolution Rates of Aqueous Ceria Observed in Situ by Liquid-Cell TEM. *ChemPhysChem* **2017**, *18* (10), 1247−1251. (c) Asghar, M. S. A.; Inkson, B.; Seal, S.; Molinari, M.; Sayle, D. C.; Mobus, G. In-situ observation of radiation physics and chemistry of nanostructured cerium oxide in water. *Mater. Res. Express* **2019**, *6* (1), 015032. (d) Zhu, G. M.; Reiner, H.; Colfen, H.; De Yoreo, J. J. Addressing some of the technical challenges associated with liquid phase S/TEM studies of particle nucleation, growth and assembly. *Micron* **2019**, *118*, 35−42. (e) Li, D. S.; Nielsen, M. H.; Lee, J. R. I.; Frandsen, C.; Banfield, J. F.; De Yoreo, J. J. Direction-Specific Interactions Control Crystal Growth by Oriented Attachment. *Science* **2012**, *336* (6084), 1014−1018.

(12) (a) Soh, M.; Kang, D. W.; Jeong, H. G.; Kim, D.; Kim, D. Y.; Yang, W.; Song, C.; Baik, S.; Choi, I. Y.; Ki, S. K.; Kwon, H. J.; Kim, T.; Kim, C. K.; Lee, S. H.; Hyeon, T. Ceria-Zirconia Nanoparticles as an Enhanced Multi-Antioxidant for Sepsis Treatment. *Angew. Chem., Int. Ed.* **2017**, *56* (38), 11399−11403. (b) Di Monte, R.; Kaspar, J. Nanostructured CeO2-ZrO2 mixed oxides. *J. Mater. Chem.* **2005**, *15* (6), 633−648.

(13) Agarwal, S.; Lefferts, L.; Mojet, B. L.; Ligthart, D. A. J. M.; Hensen, E. J. M.; Mitchell, D. R. G.; Erasmus, W. J.; Anderson, B. G.; Olivier, E. J.; Neethling, J. H.; Datye, A. K. Exposed Surfaces on Shape-Controlled Ceria Nanoparticles Revealed through AC-TEM and Water-Gas Shift Reactivity. *ChemSusChem* **2013**, *6* (10), 1898−1906.

(14) (a) Hauwiller, M. R.; Ondry, J. C.; Chan, C. M.; Khandekar, P.; Yu, J.; Alivisatos, A. P. Gold Nanocrystal Etching as a Means of Probing the Dynamic Chemical Environment in Graphene Liquid Cell Electron Microscopy. *J. Am. Chem. Soc.* **2019**, *141* (10), 4428−4437. (b) Jiang, Y. Y.; Zhu, G. M.; Dong, G. X.; Lin, F.; Zhang, H.; Yuan, J.; Zhang, Z.; Jin, C. H. Probing the oxidative etching induced dissolution of palladium nanocrystals in solution by liquid cell transmission electron microscopy. *Micron* **2017**, *97*, 22−28. (c) Jiang, Y. Y.; Zhu, G. M.; Lin, F.; Zhang, H.; Jin, C. H.; Yuan, J.; Yang, D. R.; Zhang, Z. In situ Study of Oxidative Etching of Palladium Nanocrystals by Liquid Cell Electron Microscopy. *Nano Lett.* **2014**, *14* (7), 3761−3765. (d) Sun, M.; Li, X.; Tang, Z. Q.; Wei, X. L.; Chen, Q. Constant-rate dissolution of InAs nanowires in Radiolytic water observed by in situ liquid cell TEM. *Nanoscale* **2018**, *10* (42), 19733−19741.

(15) Abellan, P.; Moser, T. H.; Lucas, I. T.; Grate, J. W.; Evans, J. E.; Browning, N. D. The formation of cerium(III) hydroxide nanoparticles by a radiation mediated increase in local pH. *RSC Adv.* **2017**, *7* (7), 3831−3837.

(16) Zhou, X. C.; Andoy, N. M.; Liu, G. K.; Choudhary, E.; Han, K. S.; Shen, H.; Chen, P. Quantitative super-resolution imaging uncovers reactivity patterns on single nanocatalysts. *Nat. Nanotechnol.* **2012**, *7* (4), 237−241.

(17) Johnston-Peck, A. C.; DuChene, J. S.; Roberts, A. D.; Wei, W. D.; Herzing, A. A. Dose-rate-dependent damage of cerium dioxide in the scanning transmission electron microscope. *Ultramicroscopy* **2016**, *170*, 1−9.

DOI: 10.1021/jacs.9b09508
J. Am. Chem. Soc. 2019, 141, 18395−18399